CHEMISTRY

Probing dissolved CO_2(aq) in aqueous solutions for CO_2 electroreduction and storage

Jiachen Li[1,2], Jinyu Guo[1,3], Hongjie Dai[1]*

Copyright © 2022 The Authors, some rights reserved; exclusive licensee American Association for the Advancement of Science. No claim to original U.S. Government Works. Distributed under a Creative Commons Attribution NonCommercial License 4.0 (CC BY-NC).

CO_2 dissolved in aqueous solutions CO_2(aq) is important to CO_2 capture, storage, photo-/electroreduction in the fight against global warming and to CO_2 analysis in drinks. Here, we developed microscale infrared (IR) spectroscopy for in situ dynamic quantitating CO_2(aq). The quantized CO_2(g) rotational state transitions were observed to quench for CO_2(aq), accompanied by increased H_2O IR absorption. An accurate CO_2 molar extinction coefficient ε was derived for in situ CO_2(aq) quantification up to 58 atm. We directly measured CO_2(aq) concentrations in electrolytes under CO_2(g) bubbling and high-pressure conditions with high spectral and time resolutions. In $KHCO_3$ electrolytes with CO_2(aq) > ~1 M, CO_2 electroreduction (CO_2RR) to formate reached >98% Faradaic efficiencies on copper (Cu_2O/Cu)–based electrocatalyst. Furthermore, CO_2 dissolution/desolvation kinetics showed large hysteresis and ultraslow reversal of CO_2(aq) supersaturation in aqueous systems, with implications to CO_2 capture, storage, and supersaturation phenomena in natural water bodies.

INTRODUCTION

Analyzing dissolved CO_2(aq) in aqueous solutions is of fundamental importance and has wide implications from environment and energy fields to consumer industries (*1*–*6*). As a greenhouse gas, excessive CO_2 emissions from burning of fossil fuels have led to negative environmental and social consequences (*5*, *6*). Absorption of CO_2(g) by aqueous solvents or natural waterbodies (*4*, *7*, *8*) is a promising approach to CO_2 capture and storage. CO_2(aq) is also a popular flavoring molecule in many types of consumer drinks (*3*, *9*, *10*). Dissolved carbon species in aqueous systems were typically probed by titration (*11*–*13*) or total carbon measurements (*12*, *14*, *15*) and analyzed by chemical equilibria analysis (*16*–*19*). Tracking of gas phase pressure (*15*), composition (*7*), and electrical (*9*, *20*) or thermal (*10*) conductivity were able to glean the kinetics of CO_2 dissolution. However, direct in situ CO_2(aq) probing with a high time resolution is rarely reported, especially under high pressures (*3*, *21*, *22*) in closed systems.

Conversion of CO_2 into fuels and value-added products via CO_2 electroreduction reaction (CO_2RR) is an attractive approach to combating climate change and closing the carbon cycle (*23*, *24*). During CO_2RR, it is widely accepted that the dissolved CO_2(aq) is the active carbon species (*25*–*28*) reduced to CO, hydrocarbons, and oxygenates (*29*–*32*), and the reduction products are influenced by CO_2(aq) concentration in the electrolytes (*30*, *32*–*35*). However, quantitative probing of CO_2(aq) to correlate with CO_2RR products is rare. For example, in widely performed CO_2RR experiments under CO_2 gas bubbling in electrolytes, CO_2(aq) was inferred from diffusion and equilibria analysis (*18*, *33*, *36*), indirect pH probing (*2*), or sampled at a given time point for total carbon (*37*), without direct kinetic measurements of CO_2(aq) in a quantitative manner.

In this work, we performed in situ Fourier transform infrared (FTIR) spectroscopy for dynamic CO_2(aq) monitoring in various aqueous systems relevant to CO_2 capture, storage, and CO_2RR conditions at up to 58 atm of pressure. A thin (<~100 μm) liquid micro-infrared (IR) cell for transmission FTIR measurements circumvented the overwhelming IR absorption of H_2O, enabling the probing of CO_2 features (*38*–*40*) over water background (*41*, *42*). Dynamic tracking of CO_2(aq) with time resolutions down to 30 s per spectrum revealed the evolution of convoluted CO_2(g) rotational-vibrational absorption bands (*40*, *43*) to a single CO_2(aq) vibrational peak (*38*, *39*), which was accompanied by significant strengthening of H_2O IR absorption especially under high pressures, suggesting considerable interactions between CO_2 and H_2O molecules that led to the quenching of CO_2 molecular rotations during aqueous dissolution. We derived a CO_2(aq) molar extinction coefficient ε of ~1.74×10^4 $M^{-1}{\cdot}cm^{-2}$ for quantitating CO_2(aq) in various solutions and beverages dynamically with a detection limit of ~1 mM (~44 mg/liter). CO_2(aq) supersaturation levels at various CO_2(g) bubbling rates in solutions were quantified. We correlated the CO_2RR products with CO_2(aq) concentrations in $KHCO_3$ electrolytes under bubbling and various pressures up to 58 atm, establishing a relation between CO_2(aq) concentration and CO_2 electrochemical conversion products. Kinetic CO_2(aq) probing over time showed faster CO_2 dissolution kinetics than desolvation in aqueous solutions, with the finding of an unexpectedly long time needed to fully reversed CO_2 supersaturation in water, which could be related to the observed CO_2 supersaturation in lakes (*44*, *45*).

RESULTS AND DISCUSSION

IR spectroscopy of CO_2 in microscale liquid cells

A micro-IR cell with two borosilicate glass (or CaF_2) windows sandwiching a thin (thickness *d* of ~10 to 100 μm, set by thin polytetrafluoroethylene spacers) aqueous layer (Fig. 1A and fig. S1) was used in our FTIR experiments. The microscale path lengths were critical to revealing CO_2 ν_3 band (C═O asymmetric stretching vibration at ~2350 cm^{-1}) (*40*, *46*, *47*) without diminished by IR adsorption of H_2O bending-libration combination mode in ~1900 to 2400 cm^{-1} region (*41*, *42*). With 0.5 M $NaHCO_3$ solution in 51.5-μm-thick micro-IR cell equilibrated under 1 atm of CO_2(g) or at continuous CO_2(g) bubbling (see Materials and Methods for details), we observed a dip in the spectrum at ~2350 cm^{-1} (IR resolution = 0.96 cm^{-1}; Fig. 1A

[1]Department of Chemistry and Bio-X, Stanford University, Stanford, CA 94305, USA. [2]Department of Materials Science and Engineering, Stanford University, Stanford, CA 94305, USA. [3]Department of Chemical Engineering, Stanford University, Stanford, CA 94305, USA.
*Corresponding author. Email: hdai@stanford.edu

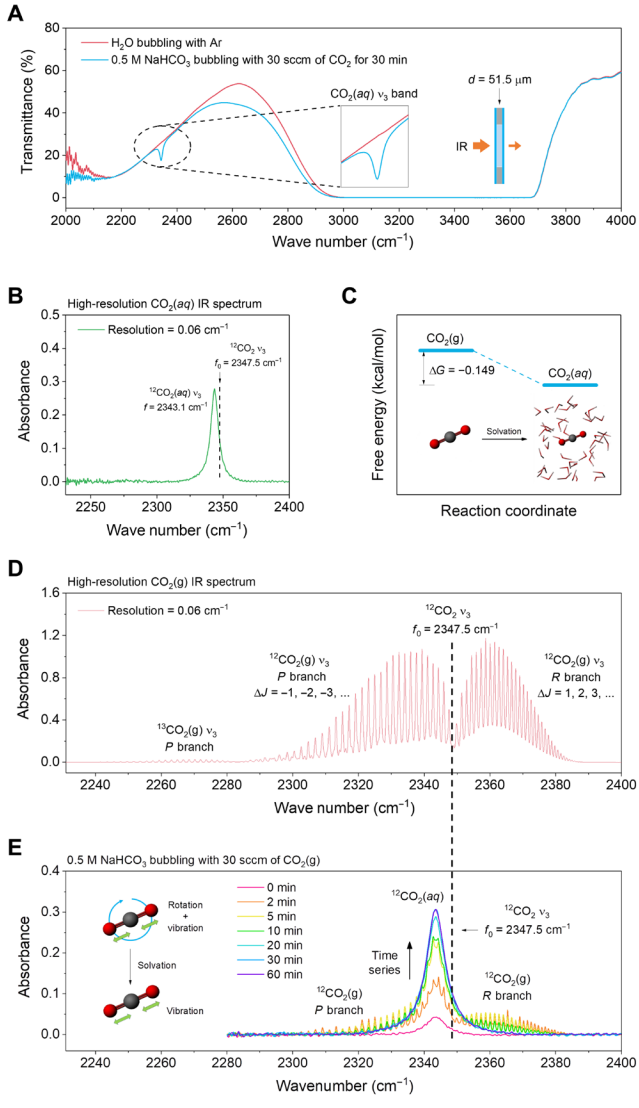


Fig. 1. CO_2 solvation in aqueous solutions monitored in micro-IR optical cells. (**A**) Transmittance FTIR spectrum (resolution = 0.96 cm^{-1}) of H_2O after bubbling with 30 sccm Ar and of 0.5 M $NaHCO_3$ solution after bubbling with 30 sccm of CO_2(g), both for 30 min. Inset: Zoom-in of 2300 to 2400 cm^{-1} range, showing CO_2(aq) ν_3 (C═O asymmetric stretching) IR absorption band; a schematic of the micro-IR cell that was used, with thin (< ~100 μm) aqueous sample films sandwiched between borosilicate glass windows for FTIR measurements. (**B**) Background subtracted CO_2(aq) ν_3 peak at f = 2343.1 cm^{-1} (resolution = 0.06 cm^{-1}) measured in water equilibrated with 1 atm of CO_2(g), showing a 4.4 cm^{-1} redshift from fundamental ν_3 vibrational frequency f_0 = 2347.5 cm^{-1} due to interactions with H_2O. (**C**) COSMO-RS simulation of Gibbs-free energy change ΔG = −0.149 kcal/mol during CO_2 solvation in atmosphere at room temperature, suggesting the high reversibility between CO_2(g) and CO_2(aq). (**D**) FTIR spectrum of $^{12}CO_2$(g) (resolution = 0.06 cm^{-1}), revealing the coupling of quantized molecular rotational transitions with C═O vibration. Sharp peaks correspond to transitions of increasing ($\Delta J > 0$, *R* branch) and decreasing ($\Delta J < 0$, *P* branch) rotational energy levels located at each side of fundamental ν_3 frequency f_0 following Boltzmann distribution. Small $^{13}CO_2$(g) signals corresponding to ~1.1% natural abundance of ^{13}C are observed near 2270 cm^{-1}. (**E**) Dynamic monitoring of CO_2 solvation in 0.5 M $NaHCO_3$ solution under 30 sccm of CO_2(g) bubbling (resolution = 0.06 cm^{-1}; see Materials and Methods for details). Sharp CO_2(g) absorption peaks diminished from ~2 min and disappeared after ~20 min, suggesting the quenching of CO_2 molecular rotations by solvating H_2O molecules during CO_2(g) to CO_2(aq) elevation.

and fig. S2). Upon background subtraction of high-resolution (0.06 cm^{-1}) spectrum, we obtained a symmetric peak at 2343.1 cm^{-1} (Fig. 1B), attributed to the main solvated carbon species CO_2(aq) (*38*–*40*, *48*, *49*). Calculation based on Conductor-like Screening Model for Real Solvents (COSMO-RS) (*50*) revealed a slight Gibbs-free energy (ΔG) decrease of 0.149 kcal/mol for CO_2 dissolution in water (Fig. 1C and see Materials and Methods for details) close to the experimental value of 0.24 kcal/mol (*51*), providing the thermodynamic driving force for CO_2(g) to CO_2(aq) (*16*, *17*). CO_2(aq) peak exhibited a 4.4 cm^{-1} redshift from fundamental CO_2 ν_3 vibrational frequency (*43*) f_0 = 2347.5 cm^{-1} (marked by dashed line in Fig. 1, B, D, and E), consistent with density functional theory (DFT) result of the decreasing trend in ν_3 frequency due to CO_2 interactions with H_2O molecules (fig. S3 and see Materials and Methods for details). For comparison, CO_2 fully hydrated to H_2CO_3 resulted in an increased ΔG of 10.254 kcal/mol based on COSMO-RS calculation (fig. S4 and see Materials and Methods for details), suggesting thermodynamically disfavored formation of H_2CO_3 and corroborating the reported H_2CO_3 concentration ≤ 0.3% of CO_2(aq) in aqueous solutions (*17*, *19*, *37*). The C═O asymmetric stretching frequency of H_2CO_3 would show a peak ~1770 cm^{-1} based on previous reports (*52*–*54*) and DFT calculation (fig. S4 and see Materials and Methods for details) but was not observed in the current work due to the low concentration and the signal was buried in the strong H—O—H bending absorption peak.

In contrast to CO_2(aq), gaseous CO_2(g) showed two broad asymmetric branches at 2336 and 2362 cm^{-1} in FTIR spectrum (resolution = 0.96 cm^{-1}; fig. S5 and see Materials and Methods for details). The branches exhibited sharp narrowly spaced peaks on the two sides of the pure ν_3 fundamental frequency f_0 = 2347.5 cm^{-1} (Fig. 1D and fig. S6) recorded at a resolution of 0.06 cm^{-1}, corresponding to the *R* branch and *P* branch of CO_2(g) rotational-vibrational spectrum with molecular rotational transitions $\Delta J > 0$ and $\Delta J < 0$, respectively (*43*). A much weaker $^{13}CO_2$(g) *P* branch (corresponding to ~1.1% natural abundance of ^{13}C) were observed in the 2500 to 2800 cm^{-1} range, with its *R* branch merging/overlapping with $^{12}CO_2$(g) *P* branch. Comparison of high-resolution CO_2(g) spectrum with the single narrow CO_2(aq) peak observed at 2343.1 cm^{-1} without *P*/*R* branch signal suggested quenching of rotational transitions and inhibition of solvated CO_2(aq) molecular rotations by the surrounding H_2O molecules.

The dynamics of CO_2 dissolution were monitored in micro-IR cell for 0.5 M $NaHCO_3$ solution under 30 standard cubic centimeter per minute (sccm) of CO_2(g) bubbling (see Materials and Methods for details). When bubbling started, the initial CO_2(aq) peak (~5 mM formed via HCO_3^- equilibria; see Materials and Methods for details) increased, accompanied by rotational *P* and *R* branches due to coexistence of CO_2(g) (Fig. 1E). The CO_2(g) *P*/*R* branch disappeared after 20 min of bubbling, leaving a symmetric single peak at 2343.1 cm^{-1} corresponding to CO_2(aq) in equilibrium with $NaHCO_3$ solution under the 30 sccm of bubbling condition. To our knowledge, this was the first time that the kinetic evolution of the rotational-vibrational IR spectrum of CO_2(g) to CO_2(aq) (Fig. 1E) were reported at a high resolution. Similar high-resolution dynamic monitoring was done in pure water and 1 M $NaHCO_3$ solutions under bubbling with 30 sccm of CO_2(g). Different to the 0.5 M $NaHCO_3$ case, we noticed that CO_2(g) signals were weaker in pure water at the same time points and disappeared after >10 min. In 1 M $NaHCO_3$, CO_2(g) signals were much stronger and persisted over >30 min (fig. S7),

suggesting the slowdown of CO_2 solvation in solutions with increasing ionic strength.

We derived a calibration curve for CO_2(aq) quantification by correlating the integrated absorbance A of CO_2(aq) ν_3 peak (peak integrated over wave number in the unit of centimeter^{-1}; Fig. 2A and fig. S8) with calculated CO_2(aq) concentrations [CO_2(aq)] in water and $NaHCO_3$ solutions equilibrated with air or 1 atm of CO_2(g) based on CO_2 dissolution equilibria (*19*) and Henry's law (*55*, *56*) (see Materials and Methods for details). High linearities in A versus solution thickness d (12.2 to 103 μm; Fig. 2B) and versus [CO_2(aq)] (Fig. 2C) were observed. The molar extinction coefficient ε of CO_2(aq) was derived from Beer's law (*57*) $A = \varepsilon \cdot [CO_2(aq)] \cdot d$ to be 1.74×10^4 $M^{-1} \cdot cm^{-2}$ (fig. S9), giving CO_2(aq) concentrations of 34.2 and 23.1 mM in 1 atm of CO_2(g) equilibrated H_2O and 0.5 M $NaHCO_3$ solutions, respectively, which were within 5% of established literature results (*55*, *56*). Note that the integrated absorbance A was found superior to peak absorbance (peak height) in yielding a constant ε independent to FTIR resolution (fig. S10). CO_2(aq) detection limit by micro-IR was determined to be ~1 mM (~44 mg/liter; see Materials and Methods for details) at an IR resolution of 0.96 cm^{-1}.

Dissolved CO_2 is an important determinant of beverage taste (*3*). CO_2 level in commercial beverages was routinely quantified in industry by tracking the electrical (*9*) or thermal (*10*) signals of released CO_2(g) from the liquids. We performed micro-IR measurements of CO_2(aq) in sparkling water, coke, grape wine, and brut champagne, applying the above calibration curve, and the various solutes in these drinks (including ethanol, sugars, minerals, and flavoring agents) did not interfere with acquiring clear and quantifiable CO_2(aq) peaks in micro-IR spectra (fig. S11 and see Materials and Methods for details). We obtained a lowest CO_2(aq) concentration of ~0.4 g/liter in grape wine, highest of ~10 g/liter in champagne, and similar concentrations of ~6 g/liter in sparkling water and coke (Fig. 2D), matching well with reported CO_2 levels (*58*, *59*) in these beverages.

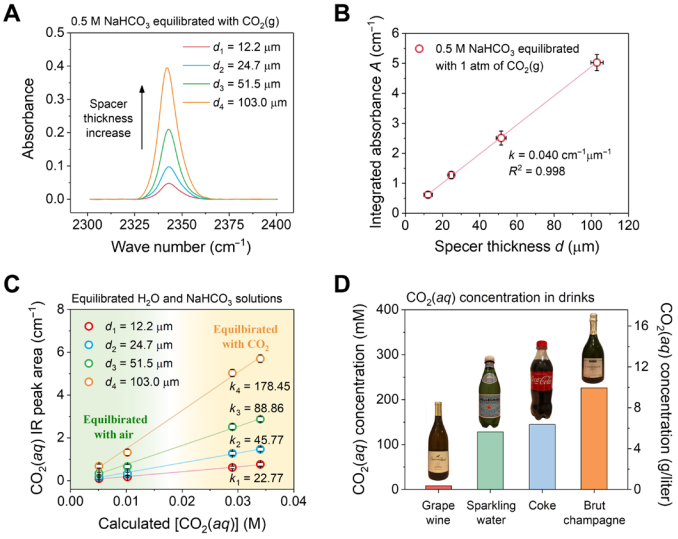


Fig. 2. CO_2(aq) quantification based on Beer's law. (**A**) Background subtracted CO_2(aq) ν_3 IR absorbance spectra (resolution = 0.96 cm^{-1}) measured in a 0.5 M $NaHCO_3$ solution equilibrated with 1 atm of CO_2(g) for 30 min in micro-IR cells with thicknesses d = 12.2, 24.7, 51.5, and 103.0 μm, respectively (gas-liquid interphase area of ~1.5 cm^2). (**B**) Integrated CO_2(aq) IR absorbance A plotted against cell thickness d, showing a high linearity (R^2 = 0.998). Error bars were obtained from three parallel measurements. (**C**) Calibration curves for CO_2(aq) integrated absorbance A versus calculated concentrations [CO_2(aq)] in micro-IR cells with different cell thicknesses d. The pure H_2O and 0.5 and 1.0 M $NaHCO_3$ solutions were equilibrated with air or 1 atm of CO_2(g) for 30 min before micro-IR measurements. Integrated absorbance A in micro-IR cells of d = 12.2, 24.7, 51.5, and 103.0 μm was correlated with [CO_2(aq)] under corresponding equilibrating condition for linear regression. Error bars were obtained from three parallel experiments. Derived CO_2(aq) molar extinction coefficient ε was 1.74×10^4 $M^{-1} \cdot cm^{-2}$ according to Beer's law. (**D**) Quantitation of CO_2(aq) in commercial drinks by micro-IR. CO_2(aq) concentration in brut champagne may be underestimated due to its high packaging pressure (see Materials and Methods for details).

Probing CO_2(aq) in solutions under CO_2 bubbling and correlation with CO_2RR

CO_2(g) bubbling into electrolytes has been widely used to provide CO_2(aq) feedstocks for CO_2RR. Our in situ micro-IR measurements revealed that with 30, 50, and 100 sccm of CO_2(g) bubbling for 30 min, equilibrium CO_2(aq) concentration in pure water reached 39.4, 50.1, and 59.9 mM, respectively, ~1.2, 1.5, and 1.8 times higher than that in water equilibrated with 1 atm of CO_2(g) without bubbling (Fig. 3A). Correspondingly, solution pH decreased from 3.8 to 3.6 when the bubbling rate increased from 0 to 100 sccm (Fig. 3A). In addition with dynamic tracking at 30 sccm of CO_2(g) bubbling (fig. S12), [CO_2(aq)] versus time were fit to phenomenological exponential functions (see Materials and Methods for details), showing a faster CO_2 dissolution kinetics under bubbling than simply equilibrating in 1 atm of CO_2(g) (time constant $t_{s1} < t_{s2}$; Fig. 3B). Note that quantitating CO_2(aq) kinetically under various bubbling conditions has not been done previously and should be considered when analyzing the CO_2RR performance.

For 0.5 M $KHCO_3$ solutions under CO_2(g) bubbling or 1 atm equilibrating, CO_2(g) peaks were observed in the initial ~10 to 20 min (fig. S13). Deconvolution of the overlapping CO_2(g) and CO_2(aq) absorption bands showed significantly slower CO_2 dissolution kinetics in the $KHCO_3$ solution than in pure water (fig. S13 and see Materials and Methods for details). After 30 min, CO_2(aq) concentration reached 29.3 mM under bubbling and 22.8 mM under 1 atm equilibrating (Fig. 3C). Similar micro-IR measurements were conducted for $KHCO_3$, KCl, K_2SO_4, and KOH solutions of various concentrations as well as seawater, revealing a general trend of CO_2(g) dissolution slowdown and CO_2(aq) equilibrium concentration decreasing when the solutions became saltier (figs. S13 to S15). These results corroborated the salting-out effect (*60*) and suggested reduced CO_2 dissolution in the presence of strong ion-H_2O interactions in aqueous solutions (*61*, *62*). The CO_2 dissolution equilibrium times and varying CO_2(aq) concentrations in different electrolytes should be considered in CO_2RR investigations.

In the commonly used 0.5 M $KHCO_3$ electrolyte for CO_2RR, we performed 30-min CO_2RR using a square-wave treated Cu_2O/Cu catalyst (SW-Cu_2O/Cu) (*30*) in an H cell after bubbling CO_2(g) at 30 sccm or after equilibrating in 1 atm of CO_2(g) environment for 30 min (see Materials and Methods for details). This catalyst was prepared under cycling square-wave oxidation/reduction potentials to form abundant Cu_2O (111) facet covering the catalyst surface (fig. S16) (*30*). When the electrolyte was under continuous bubbling through the 30-min CO_2RR reaction, the measured CO_2(aq) concentration in the solution maintained at ~30 mM (Fig. 3C), and the Faradaic efficiency (FE) of formate production was 35.7% at −1.3 V versus Ag/AgCl,

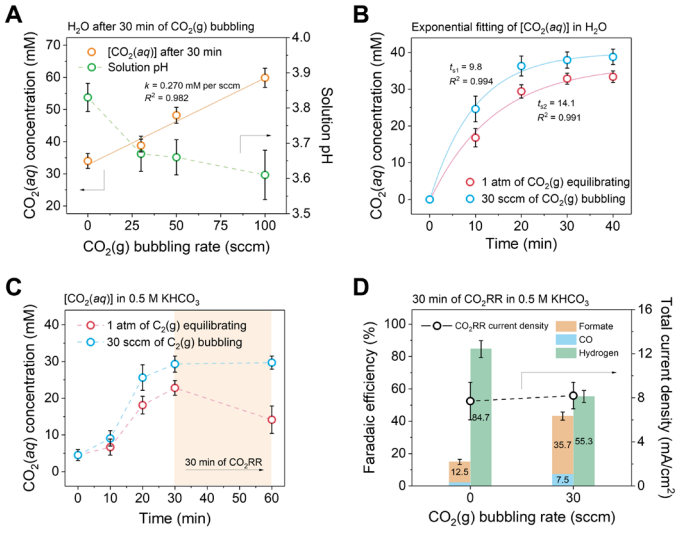


Fig. 3. Dynamic CO_2(aq) monitoring and CO_2RR. (**A**) CO_2(aq) concentrations and solution pH measured in H_2O after CO_2(g) bubbling at 0 [i.e., steady 1 atm of CO_2(g) equilibrating] to 100 sccm of for 30 min. [CO_2(aq)] showed a linearly increasing trend along CO_2(g) bubbling rate with solution pH decreasing. Error bars were obtained from three parallel experiments. (**B**) Dynamic monitoring of CO_2 solvation in H_2O under 30 sccm of CO_2(g) bubbling or 1 atm of CO_2(g) equilibrating. With [CO_2(aq)] versus time fitting by a phenomenological exponential function $y = y_0 + a * \exp(-x/t_s)$, a faster solvation kinetics and ~1.2 times higher equilibrium CO_2(aq) concentration were observed under bubbling than equilibrating in 1 atm of CO_2(g) after 40 min. Error bars were obtained from three parallel experiments. (**C**) Dynamic monitoring of CO_2 solvation in 0.5 M $KHCO_3$ solution under 30 sccm of CO_2(g) bubbling and 1 atm of CO_2(g) equilibrating. CO_2 in $KHCO_3$ solutions showed slower solvation kinetics and lower CO_2(aq) equilibrium concentrations than pure water. After 30 min of bubbling/equilibrating followed by 30 min of CO_2RR at −1.3 V versus Ag/AgCl using a SW-Cu_2O/Cu catalyst, CO_2(aq) concentration maintained in the bubbling case while significantly decreased in the equilibrating case. Error bars were obtained from three parallel experiments. (**D**) CO_2RR performance of SW-Cu_2O/Cu in 0.5 M $KHCO_3$ under 30 sccm of CO_2(g) bubbling or 1 atm of CO_2(g) equilibrating. CO_2RR started after 30 min bubbling/equilibrating at −1.3 V versus Ag/AgCl in H cell with total current densities of ~8 mA/cm^2. Higher formate production FE was obtained under the bubbling case, suggesting the strong correlation between CO_2(aq) concentration and CO_2RR performance. Error bars were obtained from three parallel experiments.

with a total current density of 8.2 mA/cm^2 (Fig. 3D and fig. S17). In contrast, CO_2(aq) in the electrolyte equilibrated under 1 atm of CO_2(g) without bubbling decreased to 14.1 mM after 30-min CO_2RR, and the corresponding formate FE decreased to 12.5% under the same CO_2RR condition (Fig. 3D). Clearly, lower CO_2(aq) concentration in the electrolyte led to a reduced FE for formate production by CO_2RR.

Probing CO_2(aq) under high pressures and correlation with CO_2RR

High CO_2(g) pressure conditions are widely used for CO_2 capture, storage, and electroreduction in aqueous solutions (*21*, *22*, *30*, *35*). However, dynamic probing of CO_2(aq) under these conditions is rarely reported, especially for CO_2RR. We equipped a micro-IR cell with a stainless steel frame and 6-mm-thick CaF_2 windows for CO_2(aq) monitoring in fully sealed aqueous samples under high CO_2(g) pressures up to 58 atm at room temperature. For pure H_2O equilibrated under 15 to 58 atm of CO_2(g) partial pressures for 30 min, FTIR spectra (d = 6.0 μm; Fig. 4A and fig. S18; see Materials and Methods for details) were used to derive CO_2(aq) concentration [CO_2(aq)] at each CO_2(g) partial pressure $p(CO_2)$ based on the integrated absorbance A (Fig. 4B) and molar extinction coefficient ε. A reciprocal fitting led to $[CO_2(aq)]^{-1} = 30.18 \times p(CO_2)^{-1} + 0.1550$ with R^2 = 0.9997 (Fig. 4C), corroborating previous experimental data and the ECO2N module analysis (an extended Henry's law) developed for CO_2 aquifers (*47*, *63*, *64*).

Under elevating CO_2(g) pressure, we observed continuous increasing of water IR absorption intensity in the whole measured range of ~1000 to 4000 cm^{-1} (fig. S18) that resulted from increased interactions between CO_2(aq) and H_2O molecules (*65*, *66*). This enhanced H_2O IR absorption was not observed in Ar-H_2O and O_2-H_2O systems (*67*) due to much weaker interactions between Ar/O_2 and H_2O molecules than CO_2.

We also measured CO_2(aq) concentration in 0.5 M $KHCO_3$ equilibrated under 15 to 58 atm of CO_2(g) and noticed lower equilibrium concentration than pure water under the same pressures. A reciprocal fitting of [CO_2(aq)] over $p(CO_2)$ gave $[CO_2(aq)]^{-1} = 43.76 * p(CO_2)^{-1} + 0.03457$ with R^2 (coefficient of determination) = 0.9996 (Fig. 4D) in the 0.5 M $KHCO_3$ electrolyte widely used for CO_2RR. Correlating with our previously reported CO_2RR to high yield formate production up to ~98.2% FE catalyzed by SW-Cu_2O/Cu[30], we found that CO_2(aq) concentration increased from 23.2 mM to 1.25 M as pressure increased from 1 to 58 atm, while the FE for formate production over 1 hour of CO_2RR increased from 27.1% to an impressive 98.2%, with the FE for H_2 generation decreased from 64.1 to ~0% (Fig. 4D). A high linearity of formate FE to CO_2(aq) concentration was observed up to ~1 M CO_2(aq) under 45 atm of CO_2(g) [independent of pH change from 7.66 to 6.01 reported earlier (*30*)], beyond which the formate FE flattened out with little further increase under 58 atm of CO_2(aq) (Fig. 4E). Since the average distance between CO_2(aq) at 1 M concentration in the electrolyte was ~1.18 nm (see Materials and Methods for details), which is on the same order as the distance between coordinatively unsaturated Cu^+ (Cu_{CUS}) (*68*) sites on Cu_2O (111) surface, this flattening was attributed to the saturation of CO_2(aq) species binding to Cu_{CUS} sites through oxygen atoms (*30*, *68*) at above 45 atm. Together, our results here confirmed that high CO_2(aq) concentrations in CO_2RR electrolyte was responsible for up to 98.2% FE of formate production on copper-based electrocatalysts under high pressures.

Probing CO_2 dissolution/desolvation hysteresis and supersaturation in aqueous solutions

Dynamic monitoring of CO_2 dissolution in water under high CO_2(g) pressures showed much faster kinetics than under 1 atm of CO_2(g) (i.e., smaller t_s; Fig. 4F). COSMO-RS simulation derived ΔG = −0.106 kcal/mol for CO_2 dissolution under 58 atm, more positive than that of −0.149 kcal/mol under 1 atm, indicating reduced thermodynamic driving forces for CO_2 dissolution at higher CO_2(aq) concentrations, which led to deviation of Henry's law from linearity in the high-pressure range (*47*, *63*). Redshifts of the H_2O bending-libration combination IR absorption band were observed under elevating CO_2(g) pressures (fig. S19), and signaling increased disruption of H_2O hydrogen bonding network when more CO_2(g) dissolved (*1*, *42*), corroborating with the positively shifted ΔG.

CO_2 supersaturation in aqueous solutions has been widely investigated (*2*, *44*, *45*, *69*), but quantitative, dynamic, and in situ monitoring of CO_2(aq) supersaturated solutions is rare. To this

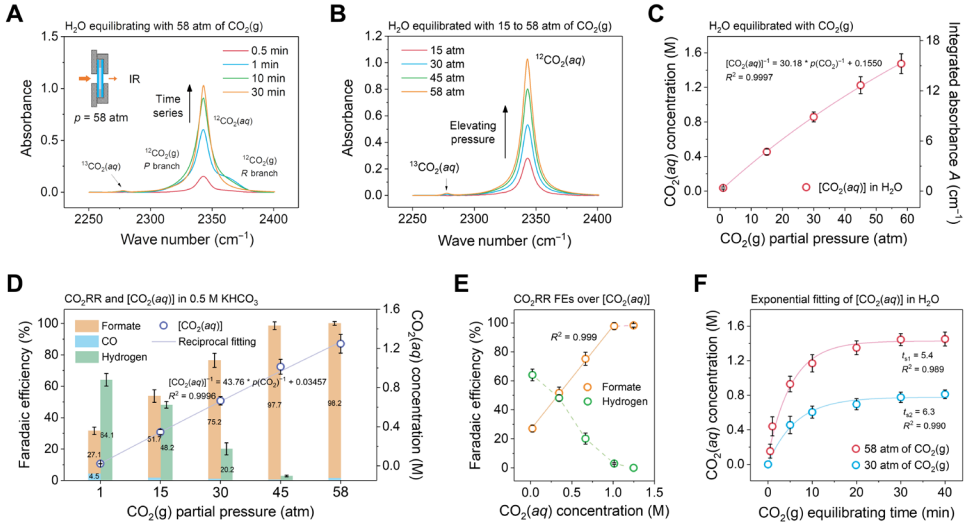


Fig. 4. Dynamic CO_2(aq) monitoring and correlation with high-pressure CO_2RR. (**A**) CO_2 ν_3 IR band dynamic evolution in H_2O under 58 atm of CO_2(g) (resolution = 0.96 cm^{-1}, d = 6 μm, and gas-liquid interphase ~1.5 cm^2). $^{12}CO_2$(g) branches diminished from ~1 min, with tiny $^{13}CO_2$(aq) signals observed. Inset: Micro-IR cell equipped with stainless steel frame for high pressures. (**B**) CO_2(aq) ν_3 IR spectra of H_2O equilibrated with 15 to 58 atm of CO_2(g) for 30 min (resolution = 0.96 cm^{-1} and d = 6.0 μm), showing stronger absorbance at higher pressures. (**C**) CO_2(aq) quantification calibration curve under 1 to 58 atm. Measured CO_2(aq) concentration was correlated with pressure $p(CO_2)$, affording a reciprocal fitting $[CO_2(aq)]^{-1} = 30.18 * p(CO_2)^{-1} + 0.1550$ with $R^2 = 0.9997$, closely agreeing with ECO2N model (*47*, *63*). Error bars were obtained from three parallel experiments. (**D**) $[CO_2(aq)]$ in 0.5 M $KHCO_3$ under various pressures correlating with SW-Cu_2O/Cu CO_2RR performances. A reciprocal fitting of measured CO_2(aq) concentration resulted in $[CO_2(aq)]^{-1} = 43.76 * p(CO_2)^{-1} + 0.03457$ with $R^2 = 0.9996$. With CO_2(aq) increasing from 0.0232 to 1.25 M along pressure, formate FE increased from 27.1 to 98.2%, and H_2 decreased from 64.1 to 0% as previously reported (*30*). Error bars were obtained from three parallel experiments. (**E**) Formate FE during CO_2RR increased linearly along $[CO_2(aq)]$ and flattened out after $[CO_2(aq)]$ > ~1 M, which potentially revealed saturated CO_2(aq) absorption on Cu_2O (111). H_2 FE decreased along $[CO_2(aq)]$ but with a weaker linearity. (**F**) CO_2 solvation kinetics in water under 30 and 58 atm of CO_2(g). With $[CO_2(aq)]$ fitting by phenomenological exponential functions, we observed faster solvation kinetics under high pressures (t_s ~5.4 and 6.3 min) than the 1 atm condition in Fig. 3B (red curve) (t_s ~14.1 min). Error bars were obtained from three parallel experiments.

end, we used micro-IR to quantitatively investigate CO_2(aq) desolvation back to CO_2(g) in supersaturated aqueous systems. Upon bubbling H_2O with 30 sccm of CO_2(g) for 30 min and exposing it to air (see Materials and Methods for details), we noticed tiny gas bubbles released from the supersaturated solution during ~3 hours of standing. Continuous probing of CO_2 ν_3 band (Fig. 5A) found that CO_2(aq) concentration in the solution decreased from 39.9 mM (0.0721% in molar fraction) to 17.2 mM [14 μM, i.e., the equilibrium level of CO_2(aq) in 1 atm of air] in 3 hours, still in a highly supersaturated state. This process was accompanied by the solution pH increase from 3.71 to 5.67 (Fig. 5B). CO_2 solvation and desolvation in aqueous systems are a complex process with solute effects and mass transport adding more complexities (*70*). We used exponential functions as phenomenological fittings of CO_2 solvation/desolvation kinetics in the time frame of 0 to a few hours to glean the solvation/desolvation speeds in various cases. By fitting $[CO_2(aq)]$ versus time to an exponential function (R^2 = 0.985), we observed a much slower desolvation kinetics than dissolution of CO_2 molecule in water (t_{ds} = 46.1 min > t_s = 9.8 min).

We observed that it is much slower to reverse CO_2(aq) supersaturation in pure water than in seawater (Fig. 5C). Upon exposure to air after CO_2 bubbling, the CO_2(aq) micro-IR signal in seawater decreased from 29.7 mM (0.0526% in molar fraction) (*71*) to below detection limit after 3 days; however, in pure water, there was still a measurable ~1.1 mM CO_2(aq) after 10 days, which was reduced to baseline only by boiling the solution (Fig. 5C). The observed CO_2 hysteresis (fast dissolution and slow desolvation) and very slow supersaturation reversal in water could be related to the observed supersaturation of dissolved CO_2 levels in freshwater lakes (*44*, *45*), more so than that in oceans (*72*). Note that slower CO_2(aq) desolvation kinetics than dissolution were also observed in $KHCO_3$ solutions and water-equilibrated with high-pressure CO_2(g) (fig. S20).

Last, we measured CO_2(aq) desolvation kinetics in beverages including sparkling water, grape wine, coke, and brut champagne upon opening seals, and the derived desolvation time constants were t_{ds} = 22.5, 15.5, 9.6, and 7.4 min, respectively (fig. S20 and see Materials and Methods for details). In general, compared with 1 atm of CO_2(g) equilibrated pure water, we observed accelerated CO_2(aq) desolvation kinetics for all the rest solutions and conditions tested (Fig. 5D), suggesting decreased favorability of CO_2 dissolution in the presence of salts/ions, sugar, alcohol, and other solutes (even including solvated CO_2 itself). That is, the solvated solutes in aqueous solutions outcompeted the dissolution of CO_2(g). Interactions of these solutes with H_2O were reflected by obvious redshifts of H_2O bending-libration combination band from f = 2144 cm^{-1} (for pure water with no solute) (Fig. 5E and fig. S21), suggesting weakened hydrogen bonding network in the presence of solvated solutes (*42*) that led to disfavored CO_2-H_2O molecular interactions slowing down CO_2 dissolution (Fig. 3, B and C, and fig. S13) and accelerating desolvation (Fig. 5, C and D, and fig. S20).

In summary, IR spectroscopy through <100-μm-thick aqueous solutions allowed in situ dynamic CO_2(aq) quantitation and dissolution/desolvation kinetics probing in various aqueous systems important to CO_2 capture, storage, electroreduction, and environmental monitoring. High-resolution spectral kinetic evolution from CO_2(g) to CO_2(aq) were obtained. An accurate CO_2(aq) molar extinction

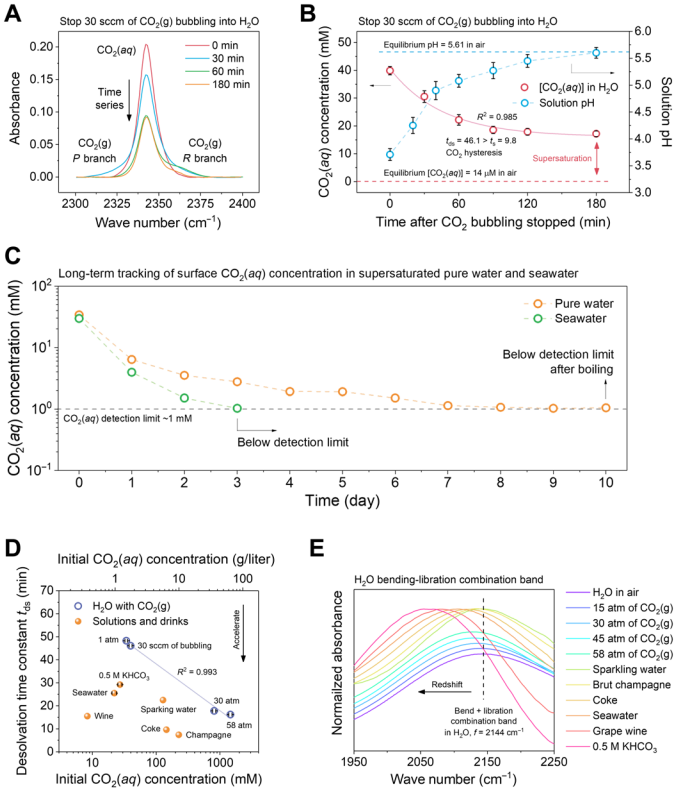


Fig. 5. Dynamic monitoring of CO_2(aq) desolvation in aqueous solutions. (**A**) CO_2 ν_3 IR band dynamic evolution in H_2O after CO_2(g) bubbling stopped and solution exposed to air (resolution = 0.96 cm^{-1}, d = 51.5 μm, and gas-liquid interphase ~1.5 cm^2). CO_2(aq) absorbance decreased and CO_2(g) appeared over time, suggesting CO_2 desolvation from water. (**B**) CO_2 desolvation in supersaturated water after bubbling stopped. With pH increasing from 3.71 to 5.67 (near equilibrium) over 3 hours standing in air, [CO_2(aq)] decreased from 40 to 17 mM, far from reversing supersaturation. [CO_2(aq)] evolution fitting by $y = y_0 + a$ * exp ($-x/t_{ds}$) suggested slower desolvation kinetics than solvation (t_{ds} = 46.1 min > t_s = 9.8 min, CO_2 hysteresis). Error bars were obtained from three parallel experiments. (**C**) Surface [CO_2(aq)] long-term tracking in supersaturated water and seawater. While [CO_2(aq)] in seawater decreased below 1 mM (detection limit) after 3 days standing in air, ~ 1.1 mM CO_2(aq) was still observed in water after 10 days and was only removable by boiling, suggesting slow desolvation in water and implying the widely observed CO_2 level difference between surface lakes and oceans. (**D**) With t_{ds} plotted versus initial equilibrium [CO_2(aq)] in H_2O (conditions indicated), seawater and $KHCO_3$ [1 atm of CO_2(g)], and commercial beverages (under/near packaged pressures), we noticed slower desolvation in H_2O (purple line/points) than all other solutions and beverages (orange points). (**E**) Bending-libration combination IR absorption of water [in air and 15 to 58 atm of CO_2(g)], seawater and $KHCO_3$ (in air), and commercial beverages (under/near packaged pressures) (resolution = 0.96 cm^{-1}; absorbance normalized for clear comparison). Systematic redshifts from H_2O bending-libration peak at 2144 cm^{-1} in air revealed weakening of hydrogen bonding network in all solute-rich solutions, where strong solute-H_2O interactions outcompeted CO_2 solvation and accelerated desolvation.

coefficient ε was determined to be 1.74 × 10^4 M^{-1}·cm^{-2}, which could facilitate CO_2(aq) quantitation by other researchers. Electrochemical CO_2RR on our Cu_2O/Cu catalyst showed strong correlations to CO_2(aq) concentration in the commonly used $KHCO_3$ electrolyte under bubbling and high-pressure conditions, exhibiting a high linearity of formate FE over CO_2(aq) until a saturation point of ~1 M CO_2(aq). The kinetics of CO_2 dissolution/desolvation were determined dynamically with a high time resolution down to 30 s in various solutions, revealing significant CO_2 hysteresis (faster solvation and slow desolvation) in aqueous systems. CO_2 dissolution slowed down, and desolvation accelerated when solutions became saltier or contained more solutes due to stronger solute (salts/ions, sugar, alcohol, etc.)—H_2O interactions than CO_2-H_2O interactions and the interruption of H_2O-hydrogen bonding network. We also observed that > 10 days, and unexpectedly long time, were needed to reverse CO_2(aq) supersaturation in water compared to ~3 days in seawater.

MATERIALS AND METHODS

Transmission FTIR spectroscopy and micro-IR optical cell

Transmission FTIR spectra of all liquid samples were obtained on a Nicolet iS50 FTIR Spectrometer using the micro-IR cell connecting with a sample reservoir (fig. S1). Borosilicate glass disc windows for the cell were purchased from McMaster-Carr Supply Company. The stainless steel cell frame, CaF_2 disc windows, and PTFE spacers for the cell were purchased from Harrick Scientific Products Inc. The stainless steel frame was screwed tightly with O-rings onto the cell windows to ensure good sealing under high pressures. During FTIR measurements, the optical cell was fixed in the FTIR chamber with continuous N_2 purging at 30 standard cubic feet per hour (scfh). Background subtraction was applied before sample testing to exclude the IR absorption of instrument, gas phase in the FTIR chamber, and cell windows (fig. S2).

FTIR measurements of CO_2(g)

We purged FTIR chamber by 30 scfh N_2 for >2 hours to remove air from the chamber. Then, with continuous N_2 purging, we flowed CO_2(g) into the chamber at 10 sccm for 5 min and recorded IR spectra at resolutions of 0.06 and 0.96 cm^{-1}.

Micro-IR measurements of $NaHCO_3$ solutions equilibrating with air

Five milliliters of 0.5 and 1.0 M $NaHCO_3$ solutions were prepared and transferred into 15-ml vials with gas-liquid interphase area of ~1.5 cm^2, and the headspace in the vials was filled with air. After standing still for 1 hour, 0.5 ml of top surface liquid samples in the vials was transferred by pipette into the micro-IR optical cell, with 1.1-mm-thick borosilicate glass windows and 12.2-, 24.7-, 51.5-, and 103.0-μm-thick PTFE spacers. This sampling process was finished in ~15 s to avoid potential changes in the liquid samples. FTIR spectra were recorded at a resolution of 0.96 cm^{-1}.

Micro-IR measurements of H_2O, seawater, $NaHCO_3$, and $KHCO_3$ solutions equilibrating with 1 atm of CO_2(g)

Five milliliters of deionized water, seawater (collected in November 2020 from San Gregorio State Beach, California, US), 0.5 and 1.0 M $NaHCO_3$ solutions, and 0.5 M $KHCO_3$ solution were prepared and transferred into 15-ml vials with gas-liquid interphase area of ~1.5 cm^2, and the headspace in the vials was filled with 1 atm of CO_2(g). After every 10 min, 0.5 ml of top surface liquid samples in the vials was transferred by pipette into the micro-IR optical cell, with 1.1-mm-thick borosilicate glass windows and 12.2-, 24.7-, 51.5-, 103.0-, and 204.2-μm-thick PTFE spacers. This sampling process was finished in ~15 s to avoid potential changes in the liquid samples, and CO_2(g) was refilled into the headspace of the vials after sampling. FTIR spectra were recorded at resolutions of 0.06, 0.24, and 0.96 cm^{-1}.

Micro-IR measurements of H_2O, $NaHCO_3$, $KHCO_3$, KCl, K_2SO_4, and KOH solutions under CO_2(g) or Ar bubbling

Five milliliters of deionized water; 0.5 and 1 M NaHCO3 solutions; 0.1, 0.5, 1.0, and 2.0 M KHCO3 solutions; 0.1, 0.5, 1.0, and 2.0 M KCl solutions; 0.05, 0.25, and 0.5 M K2SO4 solutions; and 0.1, 0.5, 1.0, and 2.0 M KOH solutions were prepared and transferred into the sample reservoir connected with micro-IR optical cell (gas-liquid interphase area of ~1.5 cm^2; fig. S1). With a CO_2(g) or Ar tubing reaching deep inside the reservoir, we kept valve V_2 closed and bubbled solutions with 30, 50, and 100 sccm of CO_2(g) or Ar. After every 10 min, valve V_2 and V_3 were opened for the CO_2(g) bubbled liquid entering and filling the 51.5-μm-thick micro-IR cell equipped with 1.1-mm-thick borosilicate glass windows. The valves were quickly closed after >300 μl of liquid flowed out of V_3 (for flushing the channels with fresh samples), and FTIR spectra were then recorded at resolutions of 0.06 and 0.96 cm^{-1}. The time it took for CO_2(g) vibration-rotation signatures disappearing from the spectra indicated the time of CO_2(g) bubbles evolving to solvated CO_2(aq) measured in the spectra.

Micro-IR measurements of sparkling water, coke, grape wine, and brut champagne

Since sparkling water (500 ml; S.Pellegrino Sparkling Natural Mineral Water, PRD 02.12.21 02), coke (500 ml; Coca-Cola Original Taste, AUG1621UVD1249), and brut champagne (750 ml; Kirkland Signature Champagne Brut, MA 3761-01-00666) were packed under pressures higher than 1 atm, we stored these drinks at 4°C for 24 hours before transferring 0.5 ml of them into 12.2-μm-thick micro-IR cell equipped with 6-mm-thick CaF_2 windows and quickly sealed the cell within ~30 s of opening the cooled drinks to minimize escaping of dissolved CO_2. After ~5 to 10 min of the liquids warming to room temperature, FTIR spectra were recorded at a resolution of 0.96 cm^{-1}. CO_2 solubility increases by ~2 times in water with temperature decreasing from 25° to 4°C (*73*); however, the measured CO_2(aq) concentration in carbonated drinks, especially champagne, could still be underestimated due to the very high concentration of CO_2(aq) and some inevitable escaping during sample transfer. For the measurement of grape wine (750 ml; Sparrow Hawk 2018 Reserve Chardonnay Napa Valley, 2107 B3 1 20190227 17 41), 0.5 ml of sample was transferred into the micro-IR cell without cooling, and FTIR spectrum was recorded at a resolution of 0.96 cm^{-1}.

Preparation of SW-Cu_2O/Cu electrode

A constant oxidation current of 5 mA/cm^2 was applied on Cu foil (99.999%, 1 cm by 1 cm; Thermo Fisher Scientific) with graphite as counter electrode in an electrolyte consisting of 0.375 M NaOH, 0.236 M Na_2CO_3, and 0.066 M Na_2SiO_3. After 15 min of oxidation, the foil was transferred into 25% H_2SO_4 and soaked for 2 hours to remove the surface oxidation layer. Then, the Cu foil was washed by ultrapure water for three times before usage. A typical square-wave redox cycling was conducted in an H-type glass cell, with two electrolyte zones being separated by a Nafion 117 membrane (Chemours, DuPont). The electrolyte contained 2.3 M lactic acid and 3.2 M KOH at 40°C water bath, with the saturated calomel electrode (SCE) being used as reference electrode and graphite being used as counter electrode. For a typical synthesis of SW-Cu_2O/Cu, the oxidation and reduction potentials were set to be −0.45 and −0.75 V (versus SCE), with an alternating frequency of 5 Hz and a cycling time of 0.5 hours. As-prepared SW-Cu_2O/Cu electrode was rinsed by ultrapure water and stored in vacuum before CO_2RR.

Characterization of the SW-Cu_2O/Cu catalyst

The morphology of as-prepared SW-Cu_2O/Cu was characterized using a field-emission scanning electron microscope (JEOL JSM6335) operating at 20 kV. Annular dark-field transmission electron microscopy measurements of a single nanoparticle on the sample was carried out on a Nion HERMES-100.

Electrochemical measurements and CO_2RR product analysis

Electrochemical measurements were carried out in a three-electrode H-type glass cell connected to an electrochemical workstation (CHI 760E). During the CO_2RR testing, SW-Cu_2O/Cu electrode was used as the working electrode, silver/silver chloride electrode (Ag/AgCl) as reference electrode, and carbon paper (1 cm by 3 cm; Sigracet SGL 39 BC) as counter electrode. With 0.5 M $KHCO_3$ solutions as electrolyte, the anodic and cathodic zones were separated by a neutralized Nafion 117 film (Fuel Cell Store). For CO_2RR under 30 sccm of CO_2(g) continues bubbling, the gaseous outlet in cathodic zone was connected to a gas chromatograph (SRI multiple gas analyzer no. 5) for online gaseous product analysis. In addition, for the nonbubbling (1 atm equilibrating) case, gas samples were collected by a syringe from the headspace of sealed cathodic zone after the 30-min reaction at −1.3 V versus Ag/AgCl and then injected into the gas chromatograph. For liquid product analysis, 0.2 ml of catholyte was collected, and one-dimensional 1H nuclear magnetic resonance (NMR) was performed on Inova 600-MHz NMR spectrometer using a water suppression method.

Micro-IR measurements of 0.5 M $KHCO_3$ solutions after CO_2RR

After 30 min of CO_2RR in H cell, 0.5 ml of liquid samples was collected from the cathodic zone (near cathode surface) and transferred by pipette into the micro-IR optical cell with 1.1-mm-thick borosilicate glass windows and 51.5-μm-thick PTFE spacer. This sampling process was finished in ~15 s to avoid potential changes in the liquid samples. FTIR spectra were recorded at a resolution of 0.96 cm^{-1}.

Micro-IR measurements of H_2O and 0.5 M $KHCO_3$ equilibrating with high-pressure CO_2(g)

Deionized water or 0.5 M $KHCO_3$ solutions (2 ml) were transferred into the sample reservoir connected with micro-IR optical cell (with 6-mm CaF_2 windows and cell thickness d = 6.0 μm; fig. S1). The stainless steel cell frame was screwed tightly with O-rings onto CaF_2 windows to ensure good sealing under high pressures. With valve V_2 opened, V_3 closed, and V_1 connected to CO_2 cylinder, 15 to 58 atm of CO_2(g) were applied to the reservoir with a gas-liquid interphase area of ~1.5 cm^2. IR spectra were recorded from 0.5 to 30 min at a resolution of 0.96 cm^{-1}.

Micro-IR measurements of CO_2 desolvation in H_2O, seawater, and 0.5 M $KHCO_3$ solution after bubbled by CO_2(g) or equilibrated with 1 atm of CO_2(g) and from commercial drinks

The liquid [5 ml; saturated with CO_2(aq) under respective conditions] was stored in 15-ml vials with the headspace filled with air (gas-liquid interphase area of ~1.5 cm^2). At various times after standing for

20 to 180 min, 0.5 ml of top surface liquid samples in the vials was transferred by pipette into the micro-IR optical cell, with 1.1-mm-thick borosilicate glass windows and 51.5-μm-thick PTFE spacers for measuring CO_2(aq) concentration. This sampling process was finished in ~15 s to avoid potential changes in the liquid samples. FTIR spectra were recorded at a resolution of 0.96 cm^{-1}.

Micro-IR measurements of CO_2 desolvation in H_2O after equilibrated with 30 and 60 atm of CO_2(g)

After 2 ml of H_2O was equilibrated with 30 or 60 atm of CO_2(g) for 30 min in 6.0-μm-thick micro-IR cell equipped with 6-mm-thick CaF_2 windows, we released the gas pressure, opened the sample reservoir, and exposed the liquids to air. FTIR spectra were recorded at a resolution of 0.96 cm^{-1} after 10 and 20 min of standing. We then switched the micro-IR cell to 51.5-μm-thick PTFE spacers and 1.1-mm-thick borosilicate glass windows for CO_2 desolvation monitoring after 30 to 180 min of exposure to air. This was done since CO_2(aq) decayed quickly to much lower levels in the initial ~30 min, after which switching to a thicker cell/longer optical path gave higher signals and provided more accurate quantification of CO_2(aq) at lower concentrations. FTIR spectra were recorded at a resolution of 0.96 cm^{-1}.

Long-term micro-IR measurement of surface CO_2(aq) in supersaturated pure water and seawater

Deionized water and seawater (5 ml each) were transferred into plastic tubes with a cross-section area of ~1.5 cm^2 and bubbled by 30 sccm of CO_2(g) for 30 min. The tubes were then kept together with 50 ml of deionized water in another container (for maintaining humidity) in a ~20-liter chamber filled with 1 atm of air. After every 24 hours, 0.5 ml of top surface liquid samples in the tubes was transferred by pipette into the micro-IR optical cell equipped with 1.1-mm-thick borosilicate glass windows and 51.5-μm-thick PTFE spacers. This sampling process was finished in ~15 s to avoid potential changes in the liquid samples. FTIR spectra were recorded at a resolution of 0.96 cm^{-1}. After 10 days of continues tracking, the supersaturated pure water sample was transferred into a beaker and boiled, and then the micro-IR measurement with the same setup was conducted for the last time once the sample cooled down to room temperature.

Micro-IR measurements of water, seawater, and 0.5 M $KHCO_3$ solution for probing H_2O bending-libration combination IR absorption band

Deionized water, seawater, or 0.5 M $KHCO_3$ solutions (0.5 ml) were transferred by pipette into the micro-IR optical cell equipped with 6-mm-thick CaF_2 windows and 6.0- or 12.2-μm-thick PTFE spacers. FTIR spectra were recorded at a resolution of 0.96 cm^{-1}.

Data processing of FTIR spectra

Raw FTIR spectra obtained from the instrument with a scale of transmittance T (%) on Y axis were converted to absorbance A by

$$A = -\log(T)$$

For further quantitative analysis, to obtain background subtracted CO_2 ν_3 (C═O asymmetric stretching) IR absorption bands in ~2300- to 2400-cm^{-1} range for liquid samples, baselines [interference (*74*) and H_2O bend + libration combination peaks] in absorbance spectra were fitted by polynomial functions and subtracted using OriginPro (version 2017b 9.4).

For CO_2 ν_3 bands with single CO_2(aq) peaks at 2343.1 cm^{-1}, the absorbance peaks were fitted by Voigt functions and integrated over wave number to obtain peak areas (in the unit of centimeter^{-1}) for quantification. In addition, for CO_2 ν_3 bands with convoluted CO_2(aq) and CO_2(g) signals at an IR resolution of 0.96 cm^{-1} (fig. S11), we fitted each convoluted ν_3 band with one Voigt function and two Asymmetric double Sigmoidal (Asym2Sig) functions in representing the single peak of CO_2(aq) and two asymmetric branches of CO_2(g), with fixed peak width and position parameters. CO_2(aq) peak width and position parameters were obtained from previous Voigt fitting of pure CO_2(aq) ν_3 peak in water at the same IR resolution, and CO_2(g) parameters were from the fitting of CO_2(g) FTIR spectra by Asym2Sig functions. CO_2(aq) peaks obtained from deconvolution were integrated over wave number for quantitative kinetics analysis.

Determination of detection limit in micro-IR measurements by SD analysis of parallel experiments

During micro-IR quantification of CO_2(aq), liquid samples were measured parallelly for three times, and the three integrated absorbance peak areas were averaged. The SD of the three parallel measurements was calculated by

$$\mathrm{SD} = \sqrt{\frac{1}{2} * \sum_{i=1}^{3} (x_i - \bar{x})^2}$$

where x_i refers to the integrated peak area in each parallel experiment and $\bar{x}$ refers to the average value. The detection limit φ of CO_2(aq) was then derived by

$$\varphi = 2 * \mathrm{SD}/\varepsilon$$

where ε refers to molar extinction coefficient of CO_2(aq) derived from working curve (fig. S7). Parallel measurements of 0.5 M $NaHCO_3$ solution equilibrated with air were used for determining CO_2(aq) detection limit at an IR resolution of 0.96 cm^{-1} using a 51.5-μm-thick micro-IR cell.

Calculation of equilibrium concentrations of CO_2(aq), H_2CO_3, HCO_3^-, CO_3^{2-}, H^+, and OH^- in H_2O equilibrated with air or 1 atm of CO_2(g) and in 0.5 M $NaHCO_3$ solution equilibrated with 1 atm of CO_2(g)

CO_2 dissolving in aqueous systems leads to the existing of multiple carbon species including CO_2(aq), H_2CO_3, HCO_3^-, and CO_3^{2-} in liquid phase at equilibrium states. The relationship between equilibrium concentrations of these species can be derived from the dissociation equations of carbonic acid (*17*, *19*, *30*)

$$H_2CO_3 \rightleftharpoons HCO_3^- + H^+$$

$$k_1 = ([H^+] * [HCO_3^-]) / [H_2CO_3] = 2.5 * 10^{-4}\,\mathrm{M} \quad (1)$$

$$HCO_3^- \rightleftharpoons CO_3^{2-} + H^+$$

$$k_2 = ([H^+] * [CO_3^{2-}]) / [HCO_3^-] = 4.84 * 10^{-11}\,\mathrm{M} \quad (2)$$

In addition, because of the high reversibility of conversions between H_2CO_3 and CO_2(aq), the first dissociation process of H_2CO_3 can be described with an apparent dissociation constant involving CO_2(aq) (*19*)

$$CO_2(aq) + H_2O \rightleftharpoons H_2CO_3 \rightleftharpoons HCO_3^- + H^+$$

$$k_a = ([H^+]*[HCO_3^-])/([H_2CO_3]+[CO_2(aq)]) = 4.45*10^{-7}\,M \quad (3)$$

Since aqueous solutions are electrically neutral, we have charge conservation equation of ion species in H_2O

$$[H^+] = [HCO_3^-]+2*[CO_3^{2-}]+[OH^-] \quad (4A)$$

and in sodium bicarbonate solution

$$[Na^+]+[H^+] = [HCO_3^-]+2*[CO_3^{2-}]+[OH^-] \quad (4B)$$

In addition, according to the dissociation equilibrium of water, the relationship of $[H^+]$ and $[OH^-]$ in liquid phase can be described as

$$H_2O \rightleftharpoons [H^+]+[OH^-]$$

$$k_w = [H^+]*[OH^-] = 10^{-14} \quad (5)$$

According to Henry's law, the concentration of dissolved CO_2(aq) in pure water or dilute solutions (< ~2 M) is linearly dependent on the partial pressure of CO_2(g) in the gas phase

$$[CO_2(aq)] = k_p * p(CO_2) \quad (6)$$

where $p(CO_2)$ refers to CO_2(g) partial pressure and k_p refers to Henry's constant of CO_2 in specific liquids at 25°C. For pure water, k_p = 0.034 M/atm at room temperature (*56*), and for the 0.5 M $NaHCO_3$ solution, k_p = 0.024 M/atm (*55*). Note that these constants are applicable under near atmospheric conditions and deviate under very high pressures (*47*, *64*).

On the basis above, we calculated equilibrium concentrations of species involved in CO_2 dissolving in H_2O and $NaHCO_3$ solution under air or 1 atm of CO_2(g) conditions using the dissociation equilibrium (Eqs. 1 to 3 and 5), ionic charge conservation (Eq. 4, A and B), and Henry's law (Eq. 6). MATLAB (version R2016a) codes for the calculations above are provided in Supplementary Text.

Calculation of equilibrium concentrations of CO_2(aq), H_2CO_3, HCO_3^-, CO_3^{2-}, H^+, and OH^- in 0.5 and 1.0 M $NaHCO_3$ solutions equilibrated with air

For bicarbonate or carbonate solutions equilibrating with a gas phase that has very low CO_2(g) partial pressures (such as air), species equilibria suggests CO_2(aq) mainly coming from the conversion of bicarbonate or carbonate ions instead of CO_2(g) dissolution (*17*, *19*). From Eqs. 1 and 3, we can obtain

$$[CO_2(aq)] = (1/k_a - 1/k_1)*[H^+]*[HCO_3^-] \quad (7)$$

Thus, equilibrium CO_2(aq) concentration increases with increasing bicarbonate concentration when $NaHCO_3$ solutions are equilibrating with air. Instead of applying Henry's law, we introduce a carbon conservation equation for those cases

$$[H_2CO_3]+[CO_2(aq)]+[HCO_3^-]+[CO_3^{2-}] = c(\text{carbon}) \quad (8)$$

where *c*(carbon) refers to the initial concentration of the bicarbonate or carbonate salt added for preparing the solution.

We calculated equilibrium concentrations of species involved in CO_2 dissolving in $NaHCO_3$ solutions under air based on dissociation equilibrium (Eqs. 1 to 3 and 5), ionic charge conservation (Eq. 4, A and B), and carbon conservation (Eq. 8). MATLAB codes for the calculations above are provided in Supplementary Text.

COSMO-RS calculations of Gibbs-free energy changes during CO_2 solvation

Gibbs-free energy change (ΔG) during CO_2 solvation in pure water under atmosphere and 58 atm of CO_2(g) was calculated using Amsterdam Modeling Suite (AMS) software package (version 2019.307). Geometry optimization of the CO_2 molecule was performed in Amsterdam Density Functional (ADF) package using generalized gradient approximation (GGA) in the scheme of Perdew-Burke-Ernzerhof (PBE) at triple-zeta polarized (TZP) basis sets (*75*). A single CO_2 molecule after geometry optimization was surrounded by 134 H_2O molecules introduced based on COSMO-RS (*76*) for simulating the solvated CO_2(aq) under atmosphere. Internal energy (*U*) and entropy (*S*) of CO_2 and $CO_2{\cdot}(H_2O)_{134}$ were calculated, respectively, at room temperature (*T* = 298.15 K) in the software. To derive ΔG, we assumed no volume change ($\Delta V = 0$) during CO_2 solvation

$$\begin{aligned}\Delta G &= \Delta(U + p*V - T*S)\\ &= \Delta U - T*\Delta S\\ &= (U_2 - U_1) - T*(S_2 - S_1)\end{aligned}$$

where *p* refers to the system pressure, U_1 and S_1 refer to the internal energy and entropy of CO_2, respectively, and U_2 and S_2 refer to those of $CO_2{\cdot}(H_2O)_{134}$.

For CO_2 solvation under 58 atm of CO_2(g), we assumed a uniform distribution of dissolved CO_2(aq) in equilibrated H_2O. Since equilibrium CO_2(aq) concentration in H_2O under 58 atm of CO_2(g) was derived to be 1.452 M according to the ECO2N module (*47*), an average distance *d* between two dissolved CO_2 molecules in the liquid phase at this concentration is

$$d = \sqrt[3]{\frac{1\ \text{liter}}{1.452\ \text{mol}*6.022*10^{23}\ \text{mol}^{-1}}} = 1.05\ \text{nm}$$

Thus, we introduced two CO_2 molecules (geometry optimized) of C—C atomic distance *d* = 1.05 nm in the software, with 131 H_2O molecules surrounded (based on COSMO-RS) to simulate the solvation in water. *U* and *S* of $(CO_2)_2$ and $(CO_2)_2{\cdot}(H_2O)_{131}$ were then calculated accordingly at room temperature to derive ΔG under the 58 atm condition.

DFT simulations of the redshift in CO_2 ν_3 vibrational frequency after solvation

CO_2 ν_3 (C═O asymmetric stretching) vibrational frequency before and after solvation was calculated on the basis of DFT using AMS software package. Geometry optimization of CO_2 molecule was

performed in ADF package at GGA/PBE/TZP level before the calculation of fundamental CO_2 ν_3 vibrational frequency f_0. For solvated CO_2(aq), we introduced one and four H_2O molecules around a single CO_2 molecule to simulate the solvation in liquid phase, since CO_2 with one H_2O coordinated (coordination number $n = 1$) was reported as the simplest structure of solvated CO_2(aq) and $n = 4$ as the most probable coordination according to energy analysis (*51*). We performed geometry optimizations using Grimme's dispersion correction method D3 with Becke-Jonson (BJ) damping (*77*) for simulating the weak noncovalent interactions between CO_2 and H_2O molecules during solvation. Calculations of ν_3 vibrational frequency, internal energy, and entropy of $CO_2{\cdot}H_2O$ and $CO_2{\cdot}(H_2O)_4$ molecular clusters at room temperature were performed at the same GGA/PBE-D3(BJ)/TZP level after geometry optimizations.

COSMO-RS calculations of Gibbs-free energy changes during CO_2 hydration to H_2CO_3

The ΔG during CO_2 hydration to H_2CO_3 was calculated using AMS software package. Geometry optimization of CO_2, H_2O, and H_2CO_3 molecules was performed in ADF package using GGA in the scheme of PBE at TZP basis sets. A single CO_2, H_2O, or H_2CO_3 molecule after geometry optimization was surrounded by 134 H_2O molecules introduced based on COSMO-RS for simulating corresponding solvated molecules under atmosphere. Internal energy (U) and entropy (S) of $CO_2{\cdot}(H_2O)_{134}$, $H_2O{\cdot}(H_2O)_{134}$, and $H_2CO_3{\cdot}(H_2O)_{134}$ were calculated, respectively, at room temperature ($T = 298.15$ K) in the software, and the Gibbs-free energy change during CO_2 hydration to H_2CO_3 was calculated to be: $\Delta G = \Delta U - T * \Delta S = (U_{H2CO3} - U_{CO2} - U_{H2O}) - T * (S_{H2CO3} - S_{CO2} - S_{H2O})$.

DFT simulations of C═O asymmetric stretching frequency in H_2CO_3

C═O asymmetric stretching frequency of H_2CO_3 was calculated on the basis of DFT using AMS software package. Geometry optimization and frequency calculation of H_2CO_3 molecule were performed in ADF package at GGA/PBE/TZP level at room temperature.

Phenomenological exponential fitting of CO_2 solvation/desolvation kinetics

CO_2 solvation and desolvation in aqueous systems are complicated processes, with solute effects and mass transport adding more complexities (*70*). A single function may not be able to fit the processes in the whole time scale range. We chose exponential functions for phenomenal fitting of CO_2 solvation and desolvation kinetics in the time frame of 0 to a few hours in our experiments, and the obtained time constants t_s and t_{ds} are merely convenient indicators to show the speed of CO_2 solvation and desolvation in different cases.

Absorption density of CO_2(aq) on Cu_2O (111) surface

At 45 atm of CO_2(g), equilibrium CO_2(aq) concentration in 0.5 M $KHCO_3$ solution was measured to be 1.01 M, so an average distance d between two dissolved CO_2 molecules in the liquid phase at this concentration is

$$d = \sqrt[3]{\frac{1\ \text{liter}}{1.01\ \text{mol} * 6.022 * 10^{23}\ \text{mol}^{-1}}} = 1.18\ \text{nm}$$

Since a SW-Cu_2O/Cu catalyst with abundant Cu_2O (111) facet on the catalyst surface was used in CO_2RR (*30*), and CO_2(aq) species were binding to the coordinately unsaturated Cu^+ (Cu_{CUS}) sites on the surface through oxygen atoms (*68*), we calculated the distance D between two Cu_{CUS} sites

$$D = \sqrt{2} * 0.427\ \text{nm} = 0.604\ \text{nm}$$

and noticed that $D \sim d/2$. This suggested that half of the active Cu_{CUS} sites responsible for formate production were occupied by CO_2(aq) at 45 atm in 0.5 M $KHCO_3$. Combining with the CO_2RR results that formate FE flattened out at more than 45 atm (main Fig. 4, D and E), one-half of the occupation of Cu_{CUS} sites should be a saturation level for CO_2(aq) absorption on Cu_2O (111) plane. In addition, the molecular diameter of CO_2 is 0.334 nm > $D/2$ (*78*), supporting the above calculation that one-half of the Cu_{CUS} sites alternatively occupied by CO_2(aq) is the maximum absorption density of CO_2(aq) on Cu_2O (111) surface.

SUPPLEMENTARY MATERIALS

Supplementary material for this article is available at https://science.org/doi/10.1126/sciadv.abo0399

REFERENCES AND NOTES

1. R. K. Lam, A. H. England, J. W. Smith, A. M. Rizzuto, O. Shih, D. Prendergast, R. J. Saykally, The hydration structure of dissolved carbon dioxide from x-ray absorption spectroscopy. *Chem. Phys. Lett.* **633**, 214–217 (2015).
2. P. Lobaccaro, M. R. Singh, E. L. Clark, Y. Kwon, A. T. Bell, J. W. Ager, Effects of temperature and gas-liquid mass transfer on the operation of small electrochemical cells for the quantitative evaluation of CO_2 reduction electrocatalysts. *Phys. Chem. Chem. Phys.* **18**, 26777–26785 (2016).
3. C. G. Viejo, D. D. Torrico, F. R. Dunshea, S. Fuentes, Bubbles, foam formation, stability and consumer perception of carbonated drinks: A review of current, new and emerging technologies for rapid assessment and control. *Foods* **8**, 596 (2019).
4. K. A. Mumford, Y. Wu, K. H. Smith, G. W. Stevens, Review of solvent based carbon-dioxide capture technologies. *Front. Chem. Sci. Eng.* **9**, 125–141 (2015).
5. S. C. Doney, V. J. Fabry, R. A. Feely, J. A. Kleypas, Ocean acidification: The other CO_2 problem. *Annu. Rev. Mar. Sci.* **1**, 169–192 (2009).
6. J. F. B. Mitchell, The "greenhouse" effect and climate change. *Rev. Geophys.* **27**, 115–139 (1989).
7. H. Li, Z. Tang, X. Xing, D. Guo, L. Cui, X. Mao, Study of CO_2 capture by seawater and its reinforcement. *Energy* **164**, 1135–1144 (2018).
8. M. Aresta, A. Dibenedetto, A. Angelini, Catalysis for the valorization of exhaust carbon: From CO_2 to chemicals, materials, and fuels. Technological use of CO_2. *Chem. Rev.* **114**, 1709–1742 (2014).
9. S. Teerasong, S. Chan-Eam, K. Sereenonchai, N. Amornthammarong, N. Ratanawimarnwong, D. Nacapricha, A reagent-free SIA module for monitoring of sugar, color and dissolved CO_2 content in soft drinks. *Anal. Chim. Acta* **668**, 47–53 (2010).
10. C. Descoins, M. Mathlouthi, M. Le Moual, J. Hennequin, Carbonation monitoring of beverage in a laboratory scale unit with on-line measurement of dissolved CO_2. *Food Chem.* **95**, 541–553 (2006).
11. T. E. Friedemann, A. I. Kendall, The determination of carbon and carbon dioxide. *J. Biol. Chem.* **82**, 45–55 (1929).
12. C. Z. Phak, S. B. M. Saleh, M. A. Muzammil, Comparison of total inorganic carbon (TIC) analysis with titration method analysis in determining carbon dioxide (CO_2) content of amine solvent. *IOP Conf. Ser.* **458**, 012033 (2018).
13. N. McCann, D. Phan, X. Wang, W. Conway, R. Burns, M. Attalla, G. Puxty, M. Maeder, Kinetics and mechanism of carbamate formation from CO_2(aq), carbonate species, and monoethanolamine in aqueous solution. *Chem. Eur. J.* **113**, 5022–5029 (2009).
14. I. Adeyemi, M. R. M. Abu-Zahra, I. Alnashef, Novel green solvents for CO_2 capture. *Energy Procedia* **114**, 2552–2560 (2017).
15. F. A. Chowdhury, H. Yamada, T. Higashii, K. Goto, M. Onoda, CO_2 capture by tertiary amine absorbents: A performance comparison study. *Ind. Eng. Chem. Res.* **52**, 8323–8331 (2013).
16. F. J. W. Roughton, The kinetics and rapid thermochemistry of carbonic acid. *J. Am. Chem. Soc.* **63**, 2930–2934 (1941).
17. D. M. Kern, The hydration of carbon dioxide. *J. Chem. Educ.* **37**, 14–23 (1960).
18. J. Al-Gousous, N. Salehi, G. E. Amidon, R. M. Ziff, P. Langguth, G. L. Amidon, Mass transport analysis of bicarbonate buffer: Effect of the CO_2-H_2CO_3 hydration-dehydration

kinetics in the fluid boundary layer and the apparent effective pKa controlling dissolution of acids and bases. *Mol. Pharm.* **16**, 2626–2635 (2019).
19. N. N. Greenwood, A. Earnshaw, *Chemistry of the Elements* (Butterworth-Heinemann, ed. 2, 1997), pp. 310.
20. J. W. Severinghaus, A. F. Bradley, Electrodes for blood pO_2 and pCO_2 determination. *J. Appl. Physiol.* **13**, 515–520 (1958).
21. S. Yamamoto, H. Machida, Y. Fujioka, T. Higashii, Development of chemical CO_2 solvent for high-pressure CO_2 capture. *Energy Procedia* **37**, 505–517 (2013).
22. M. K. Wong, A. M. Shariff, M. A. Bustam, Raman spectroscopic study on the equilibrium of carbon dioxide in aqueous monoethanolamine. *RSC Adv.* **6**, 10816–10823 (2016).
23. S. Xu, E. A. Carter, Theoretical insights into heterogeneous (photo)electrochemical CO_2 reduction. *Chem. Rev.* **119**, 6631–6669 (2019).
24. X. Li, J. Yu, M. Jaroniec, X. Chen, Cocatalysts for selective photoreduction of CO_2 into solar fuels. *Chem. Rev.* **119**, 3962–4179 (2019).
25. S. Zhu, B. Jiang, W. B. Cai, M. Shao, Direct observation on reaction intermediates and the role of bicarbonate anions in CO_2 electrochemical reduction reaction on Cu surfaces. *J. Am. Chem. Soc.* **139**, 15664–15667 (2017).
26. M. Dunwell, Q. Lu, J. M. Heyes, J. Rosen, J. G. Chen, Y. Yan, F. Jiao, B. Xu, The central role of bicarbonate in the electrochemical reduction of carbon dioxide on gold. *J. Am. Chem. Soc.* **139**, 3774–3783 (2017).
27. A. Olivo, E. Ghedini, M. Signoretto, M. Compagnoni, I. Rossetti, Liquid vs. gas phase CO_2 photoreduction process: Which is the effect of the reaction medium? *Energies* **10**, 1394 (2017).
28. B. Kumar, M. Llorente, J. Froehlich, T. Dang, A. Sathrum, C. P. Kubiak, Photochemical and photoelectrochemical reduction of CO_2. *Annu. Rev. Phys. Chem.* **63**, 541–569 (2012).
29. C. T. Dinh, T. Burdyny, M. G. Kibria, A. Seifitokaldani, C. M. Gabardo, P. G. de Arquer, A. Kiani, J. P. Edwards, P. D. Luna, O. S. Bushuyev, C. Zou, R. Quintero-Bermudez, Y. Pang, D. Sinton, E. H. Sargent, CO_2 electroreduction to ethylene via hydroxide-mediated copper catalysis at an abrupt interface. *Science* **360**, 783–787 (2018).
30. J. Li, Y. Kuang, Y. Meng, X. Tian, W. H. Hung, X. Zhang, A. Li, M. Xu, W. Zhou, C. S. Ku, C. Y. Chiang, G. Zhu, J. Guo, X. Sun, H. Dai, Electroreduction of CO_2 to formate on a copper-based electrocatalyst at high pressures with high energy conversion efficiency. *J. Am. Chem. Soc.* **142**, 7276–7282 (2020).
31. R. G. Mariano, K. McKelvey, H. S. White, M. W. Kanan, Selective increase in CO_2 electroreduction activity at grain-boundary surface terminations. *Science* **358**, 1187–1192 (2017).
32. X. Zhang, J. Li, Y. Y. Li, Y. Jung, Y. Kuang, G. Zhu, Y. Liang, H. Dai, Selective and high current CO_2 electro-reduction to multicarbon products in near-neutral KCl electrolytes. *J. Am. Chem. Soc.* **143**, 3245–3255 (2021).
33. Y. C. Tan, K. B. Lee, H. Song, J. Oh, Modulating local CO_2 concentration as a general strategy for enhancing C-C coupling in CO_2 electroreduction. *Joule* **4**, 1104–1120 (2020).
34. J. Li, Z. Wang, C. McCallum, Y. Xu, F. Li, Y. Wang, C. M. Gabardo, C. T. Dinh, T. T. Zhuang, L. Wang, J. Y. Howe, Y. Ren, E. H. Sargent, D. Sinton, Constraining CO coverage on copper promotes high-efficiency ethylene electroproduction. *Nat. Catal.* **2**, 1124–1131 (2019).
35. E. Bahadori, A. Tripodi, A. Villa, C. Pirola, L. Prati, G. Ramis, I. Rossetti, High pressure photoreduction of CO_2: Effect of catalyst formulation, hole scavenger addition and operating conditions. *Catalysts* **8**, 430 (2018).
36. N. Gupta, M. Gattrell, B. MacDougall, Calculation for the cathode surface concentrations in the electrochemical reduction of CO_2 in $KHCO_3$ solutions. *J. Appl. Electrochem.* **36**, 161–172 (2006).
37. H. Zhong, K. Fujii, Y. Nakano, F. Jin, Effect of CO_2 bubbling into aqueous solutions used for electrochemical reduction of CO_2 for energy conversion and storage. *J. Phys. Chem. C* **119**, 55–61 (2015).
38. L. H. Jones, E. McLaren, Infrared absorption spectra of SO_2 and CO_2 in aqueous solution. *J. Chem. Phys.* **28**, 995–995 (1958).
39. M. Falk, A. G. Miller, Infrared spectrum of carbon dioxide in aqueous solution. *Vib. Spectrosc.* **4**, 105–108 (1992).
40. D. E. Burch, D. A. Gryvnak, D. Williams, Total absorptance of carbon dioxide in the infrared. *Appl. Opt.* **1**, 759–765 (1962).
41. E. K. Plyler, N. Acquista, Infrared absorption of liquid water from 2 to 42 microns. *J. Opt. Soc. Am.* **44**, 505 (1954).
42. P. K. Verma, A. Kundu, M. S. Puretz, C. Dhoonmoon, O. S. Chegwidden, C. H. Londergan, M. Cho, The bend + libration combination band is an intrinsic, collective, and strongly solute-dependent reporter on the hydrogen bonding network of liquid water. *J. Phys. Chem. B* **122**, 2587–2599 (2018).
43. R. M. Spearrin, W. Ren, J. B. Jeffries, R. K. Hanson, Multi-band infrared CO_2 absorption sensor for sensitive temperature and species measurements in high-temperature gases. *App. Phys. B* **116**, 855–865 (2014).
44. J. J. Cole, N. F. Caraco, G. W. Kling, T. K. Kratz, Carbon dioxide supersaturation in the surface waters of lakes. *Science* **265**, 1568–1570 (1994).
45. R. Marcé, B. Obrador, J. A. Morguí, J. L. Riera, P. López, J. Armengol, Carbonate weathering as a driver of CO_2 supersaturation in lakes. *Nat. Geosci.* **8**, 107–111 (2015).
46. T. Schädle, B. Pejcic, B. Mizaikoff, Monitoring dissolved carbon dioxide and methane in brine environments at high pressure using IR-ATR spectroscopy. *Anal. Methods* **8**, 756–762 (2016).
47. T. Schädle, B. Pejcic, M. Myers, B. Mizaikoff, Portable mid-infrared sensor system for monitoring CO_2 and CH_4 at high pressure in geosequestration scenarios. *ACS Sens.* **1**, 413–419 (2016).
48. S. A. Sandford, L. J. Allamandola, The physical and infrared spectral properties of CO_2 in astrophysical ice analogs. *Astrophys. J.* **355**, 357–372 (1990).
49. S. Schaden, M. Haberkorn, J. Frank, J. R. Baena, B. Lendl, Direct determination of carbon dioxide in aqueous solution using mid-infrared quantum cascade lasers. *Appl. Spectrosc.* **58**, 667–670 (2004).
50. A. Klamt, Conductor-like screening model for real solvents: A new approach to the quantitative calculation of solvation phenomena. *J. Phys. Chem.* **99**, 2224–2235 (1995).
51. D. Jiao, S. B. Rempe, CO_2 solvation free energy using quasi-chemical theory. *J. Chem. Phys.* **134**, 224506 (2011).
52. W. Hage, K. R. Liedl, A. Hallbrucker, E. Mayer, Carbonic acid in the gas phase and its astrophysical relevance. *Science* **279**, 1332–1335 (1998).
53. C. Mitterdorfer, J. Bernard, F. Klauser, K. Winkel, I. Kohl, K. R. Liedl, H. Grothe, E. Mayer, T. Loerting, Local structural order in carbonic acid polymorphs: Raman and FT-IR spectroscopy. *J. Raman Spectrosc.* **43**, 108–115 (2012).
54. J. Bernard, R. G. Huber, K. R. Liedl, H. Grothe, T. Loerting, Matrix isolation studies of carbonic acid - the vapor phase above the β-polymorph. *J. Am. Chem. Soc.* **135**, 7732–7737 (2013).
55. C. S. Wong, P. Y. Tishchenko, W. K. Johnson, Solubility of carbon dioxide in aqueous HCl and $NaHCO_3$ solutions from 278 to 298 K. *J. Chem. Eng. Data* **50**, 817–821 (2005).
56. R. Sander, Compilation of Henry's law constants (version 4.0) for water as solvent. *Atmos. Chem. Phys.* **15**, 4399–4981 (2015).
57. D. F. Swinehart, The Beer-Lambert law. *J. Chem. Educ.* **39**, 333–335 (1962).
58. E. Ljunggren, B. Karlberg, Determination of total carbon dioxide in beer and soft drinks by gas diffusion and flow injection analysis. *J. Autom. Chem.* **17**, 105–108 (1995).
59. G. Liger-Belair, G. Polidori, P. Jeandet, Recent advances in the science of champagne bubbles. *Chem. Soc. Rev.* **37**, 2490–2511 (2008).
60. K. Onda, E. Sada, T. Kobayashi, S. Kito, K. Ito, Salting-out parameters of gas solubility in aqueous salt solutions. *J. Chem. Eng. Jpn* **3**, 18–24 (1970).
61. G. Stirnemann, E. Wernersson, P. Jungwirth, D. Laage, Mechanisms of acceleration and retardation of water dynamics by ions. *J. Am. Chem. Soc.* **135**, 11824–11831 (2013).
62. Z. S. Nickolov, O. Ozcan, J. D. Miller, FTIR analysis of water structure and its significance in the flotation of sodium carbonate and sodium bicarbonate salts. *Colloids Surf. A Physicochem. Eng. Asp.* **224**, 231–239 (2003).
63. K. Pruess, N. Spycher, ECO2N–A fluid property module for the TOUGH2 code for studies of CO_2 storage in saline aquifers. *Energy Convers. Manag.* **48**, 1761–1767 (2007).
64. L. W. Diamond, N. N. Akinfiev, Solubility of CO_2 in water from −1.5 to 100 °C and from 0.1 to 100 MPa: Evaluation of literature data and thermodynamic modelling. *Fluid Phase Equilib.* **208**, 265–290 (2003).
65. J. E. Lowder, Increase of integrated intensities of H_2O infrared bands produced by hydrogen bonding. *J. Quant. Spectrosc. Radiat. Transf.* **11**, 153–159 (1971).
66. S. Kuma, M. N. Slipchenko, K. E. Kuyanov, T. Momose, A. F. Vilesov, Infrared spectra and intensities of the H_2O and N_2 complexes in the range of the ν_1- and ν_3-bands of water. *Chem. Eur. J.* **110**, 10046–10052 (2006).
67. S. Kuma, M. N. Slipchenko, Infrared spectra and intensities of Ar-H_2O and O_2-H_2O complexes in the range of the ν3 band of H_2O. *Chem. Eur. J.* **114**, 9022–9027 (2010).
68. A. K. Mishra, N. H. de Leeuw, Mechanistic insights into the Cu(I) oxide-catalyzed conversion of CO_2 to fuels and chemicals: A DFT approach. *J. CO2 Utilization* **15**, 96–106 (2016).
69. J. T. Kraemer, D. M. Bagley, Supersaturation of dissolved H_2 and CO_2 during fermentative hydrogen production with N_2 sparging. *Biotechnol. Lett.* **28**, 1485–1491 (2006).
70. M. J. Mitchell, O. E. Jensen, K. A. Cliffe, M. M. Maroto-Valer, A model of carbon dioxide dissolution and mineral carbonation kinetics. *Proc. R. Soc. A* **466**, 1265–1290 (2009).
71. M. E. Q. Pilson, *An Introduction to the Chemistry of the Sea* (Cambridge Univ. Press, ed. 2, 2013), pp. 67.
72. J. E. Dore, R. Lukas, D. W. Sadler, M. J. Church, D. M. Karl, Physical and biogeochemical modulation of ocean acidification in the central North Pacific. *Proc. Natl. Acad. Sci. U.S.A.* **106**, 12235–12240 (2009).
73. N. Abas, N. Khan, Carbon conundrum, climate change, CO_2 capture and consumptions. *J. CO2 Utilization* **8**, 39–48 (2014).
74. T. G. Mayerhofer, S. Pahlow, U. Hubner, J. Popp, Removing interference-based effects from infrared spectra-interference fringes re-revisited. *Analyst* **145**, 3385–3394 (2020).
75. J. P. Perdew, K. Burke, M. Ernzerhof, Generalized gradient approximation made simple. *Phys. Rev. Lett.* **77**, 3865–3868 (1996).
76. A. Klamt, G. Schuurmann, COSMO: A new approach to dielectric screening in solvents with explicit expressions for the screening energy and its gradient. *J. Chem. Soc., Perkin Trans. 2* **5**, 799–805 (1993).

77. S. Grimme, S. Ehrlich, L. Goerigk, Effect of the damping function in dispersion corrected density functional theory. *J. Comput. Chem.* **32**, 1456–1465 (2011).
78. H. P. S. A. Khalil, C. K. Saurabh, M. I. Syakir, M. R. N. Fazita, A. Bhat, A. Banerjee, H. M. Fizree, S. Rizal, P. M. Tahir, *Mechanical and Physical Testing of Biocomposites, Fibre-Reinforced Composites and Hybrid Composites* (Woodhead Publishing, 2019), pp. 247.

Acknowledgments: We thank M. D. Fayer and R. Xie for helpful discussions. **Funding:** This work was supported by Deng family gift fund and Stanford Bits & Watts Initiative. Part of this work was performed at Stanford Nano Shared Facilities (SNSF), supported by National Science Foundation under award ECCS-2026822. **Author contributions:** H.D. and J.L. conceived the project ideas. J.L. and J.G. performed the experiments. J.L. and J.G. performed the calculations. J.L. and H.D. prepared the manuscript. All authors participated in data analysis and discussions. **Competing interests:** J.L., J.G., and H.D. are inventors on a provisional patent application related to this work to be filed at the U.S. Patent and Trademark Office. The authors declare that they have no other competing interests. **Data and materials availability:** All data needed to evaluate the conclusions in the paper are present in the paper and/or the Supplementary Materials.

Submitted 9 January 2022
Accepted 31 March 2022
Published 13 May 2022
10.1126/sciadv.abo0399